High-Throughput Exploration of Triple-Cation Perovskites via All-in-One Compositionally-Graded Films

Shahram Moradi, Soumya Kundu, Muhammad Awais, Yuki Haruta, Hai-Dang Nguyen, Dongyang Zhang, Furui Tan, and Makhsud I. Saidaminov

2023

This article was originally published at:
https://doi.org/10.1002/smll.202301037

Citation for this paper:

Moradi, S., Kundu, S., Awais, M., Haruta, Y., Nguyen, H., Zhang, D., Tan, F., & Saidaminov, M. I. (2023). High-throughput exploration of triple-cation perovskites via All-in-one compositionally-graded films. *Small*, *19*(42). https://doi.org/10.1002/smll.202301037

High-Throughput Exploration of Triple-Cation Perovskites via All-in-One Compositionally-Graded Films

*Shahram Moradi, Soumya Kundu, Muhammad Awais, Yuki Haruta, Hai-Dang Nguyen, Dongyang Zhang, Furui Tan, and Makhsud I. Saidaminov**

Many devices heavily rely on combinatorial material optimization. However, new material alloys are classically developed by studying only a fraction of giant chemical space, while many intermediate compositions remain unmade in light of the lack of methods to synthesize gapless material libraries. Here report a high-throughput all-in-one material platform to obtain and study compositionally-tunable alloys from solution is reported. This strategy is applied to make all $Cs_xMA_yFA_zPbI_3$ perovskite alloys (MA and FA stand for methylammonium and formamidinium, respectively), in less than 10 min, on a single film, on which 520 unique alloys are then studied. Through stability mapping of all these alloys in air supersaturated with moisture, a range of targeted perovskites are found, which are then chosen to make efficient and stable solar cells in relaxed fabrication conditions, in ambient air. This all-in-one platform provides access to an unprecedented library of compositional space with no unmade alloys, and hence aids in a comprehensive accelerated discovery of efficient energy materials.

1. Introduction

The progress of many important technologies such as solar cells, light-emitting diodes, batteries, superconductors, and thermoelectrics rely on how fast materials are discovered or developed. Because the best materials are often a blend of multiple components, high-throughput experimentations (HTEs),[1–33] both for making and studying mixtures/alloys, have recently gained major attention.[2] However, state-of-art HTEs are unfortunately able to make only a fraction of possible compositions and then employ machine learning algorithms to extrapolate to unmade compositional space.[25,33] Being able to make all possible alloys simultaneously, in one batch, would provide access to unprecedentedly large material libraries, but this remains a challenge. One field which would benefit from HTE is halide perovskites, a family of semiconductors that offers an unusually long charge-carrier diffusion length for solution-processed materials.[34–38] Halide perovskites hence were widely researched for a range of optoelectronics. Particularly, perovskite solar cells (PSCs)[39–42] showed unprecedented rapid progress, in large part due to perovskite compositional engineering. For instance, formamidinium lead triiodide ($FAPbI_3$) perovskite is an important photovoltaic absorber as it has an optimal bandgap of ≈1.5 eV; but it unfortunately easily transforms to a different polymorph with an undesired large bandgap of 2.5 eV. Stabilizing $FAPbI_3$ by alloying with different cations and/or halogens led to record-breaking PSCs.[43] However, this process has hitherto relied on a fragmentary approach, when only a fraction of enormous compositional space was made and studied. We recently reported compositionally–graded films (CGFs) which provide a continuous combinatorial combination of all potential binary alloys.[2] As an example, we demonstrated CGF of $MAPbI_3$ and $MAPbBr_3$.[4] It is now essential to develop platforms that allow experimentally exploring (making and studying) all multinary alloys, particularly due to further needs for commercially-relevant stable perovskites.[5,6,27,30,44–49]

Here we report a strategic composition–integrated platform where all possible ternary alloys can be obtained at once from solution in less than 10 min. We apply our approach to make $Cs_xMA_yFA_zPbI_3$ perovskite alloys on a single film, on which

---

S. Moradi, M. Awais, M. I. Saidaminov
Department of Electrical and Computer Engineering
University of Victoria
3800 Finnerty Rd, Victoria, BC V8P 5C2, Canada
E-mail: msaidaminov@uvic.ca

S. Kundu, Y. Haruta, H.-D. Nguyen, D. Zhang, M. I. Saidaminov
Department of Chemistry
University of Victoria
3800 Finnerty Rd, Victoria, BC V8P 5C2, Canada

F. Tan
Key Laboratory of Photovoltaic Materials
Henan University
Kaifeng 475004, P. R. China

M. I. Saidaminov
Centre for Advanced Materials and Related Technologies (CAMTEC)
University of Victoria
3800 Finnerty Rd, Victoria, BC V8P 5C2, Canada

The ORCID identification number(s) for the author(s) of this article can be found under https://doi.org/10.1002/smll.202301037

DOI: 10.1002/smll.202301037

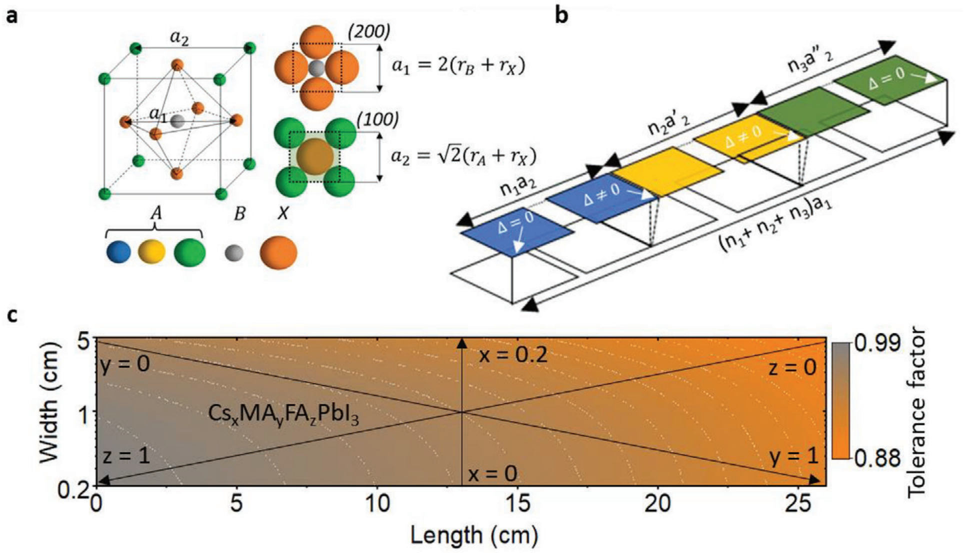

Figure 1. Computing effective tolerance factor of triple cation perovskites. a) Schematic of perovskite cubic unit cell with ABX_3 composition; b) 1D superlattice of ABX_3 with triple A-cations showcasing accumulated offset ($\Delta = |a_2 - a_1|$); c) computed effective Goldschmidt tolerance factor for triple cation perovskites for $0.88 < t_{\text{eff}} < 1$.

we then study 520 unique material compositions via a high-throughput optical characterization tool. In situ stability mapping of all these alloys in a high-humidity environment allows for finding a range of ternary perovskites that remain intact under these harsh conditions. We observe the unique role of each component—organic cations aid in stabilizing perovskite structure, while an inorganic cation (cesium)—in the crystallization of pin-hole free films. With this accelerated material discovery platform, we then make solar cells using perovskites from the defined humidity-stable range and test the unencapsulated devices at elevated temperatures. We reveal three distinct degradation pathways in operational devices as a function of composition: 1) mixed-halide mixed-cation PSCs degrade by losing photocurrent and photovoltage; 2) single-halide organic-rich PSCs lose either photocurrent or photovoltage; and 3) single-halide inorganic-rich PSCs show the longest operational stability.

2. Results and Discussion

In a cubic perovskite structure of ABX_3 composition, the lattice parameter can be extracted from two Miller planes (**Figure 1**a): from (200) plane in which case the unit cell (a_1) is comprised of two radii of *B* and *X*; and from (100) plane in which case the unit cell (a_2) is comprised of cathetus of the right-angle triangle whose hypotenuse is comprised of two radii of *A* and *X*. The ratio of a_2/a_1, known as Goldschmidt tolerance factor (t), should be close to unity to form a stable perovskite with no/little structural distortion.[50]

We applied Goldschmidt's theory to assess the structural stability of iodide triple-A–cation perovskites, $Cs_xMA_yFA_zPbI_3$, where $x + y + z = 1$. Note that we did not consider mixed halides, as they are known,[4] also shown below, to be prone to phase segregation. If the ternary perovskite is represented as a 1D superlattice of $N = n_1 + n_2 + n_3$ unit cells (Figure 1b), where n_1, n_2, and n_3 define the ratio of A-site cations ($x = n_1/N$, $y = n_2/N$, $z = n_3/N$), then the effective tolerance factor is $t_{\text{eff}} = (n_1a_2 + n_2a'_2 + n_3a''_2)/Na_1$, where a_2, a'_2, and a''_2 are (100) lattice constants with Cs, MA, and FA, respectively (Note S1, Supporting Information). Taking $t_{\text{eff}} > 0.88$ as a criterion to form a stable cubic perovskite structure,[51] we defined the compositional range of $Cs_xMA_yFA_zPbI_3$ to be $0 < x < 0.2$, $0 < y < 1$, and $0 < z < 1$ (Figure 1c).

We then sought to synthesize the ternary alloys of the defined compositional range. Making them by traditional "fragmentary" approach would not only be time-consuming (e.g., 10^3 compositions only for 10% increments), but would also miss many intermediate compositions. We recently demonstrated a high-throughput approach to synthesize all possible binary alloys on a single thin film, which we termed compositionally-graded film (CGF),[4] via in situ compositional change of deposition ink. However, our original CGF approach was limited to only binary systems.

We hence upgraded our approach to be able to achieve ternary CGF (t-CGF) by coating gradient films of three ingredients sequentially, but with varying gradient directions (**Figure 2**a). We fabricated individual graded films by slot-die coating (Note S2, Supporting Information). To achieve t-CGFs, we deposited three layers sequentially, on top of each other, with varying thicknesses to cover the entire compositional space with asymmetric combinatorial ratios (Note S3 and Figure S1, Supporting Information).

We fabricated the t-CGF on a substrate of 130 cm^2 area (5 cm width and 26 cm length). Figure 2b provides the detailed three-step fabrication conditions of $Cs_xMA_yFA_zPbI_3$ t-CGFs. First, $CsPbI_3$ film was deposited by a tilted slot-die head to achieve a thickness gradient across the width of the substrate (Figure S2a,b, Supporting Information). $MAPbI_3$ was then deposited on top of $CsPbI_3$ film by an in situ decrease of ink concentration to achieve a thickness gradient across the length of the substrate

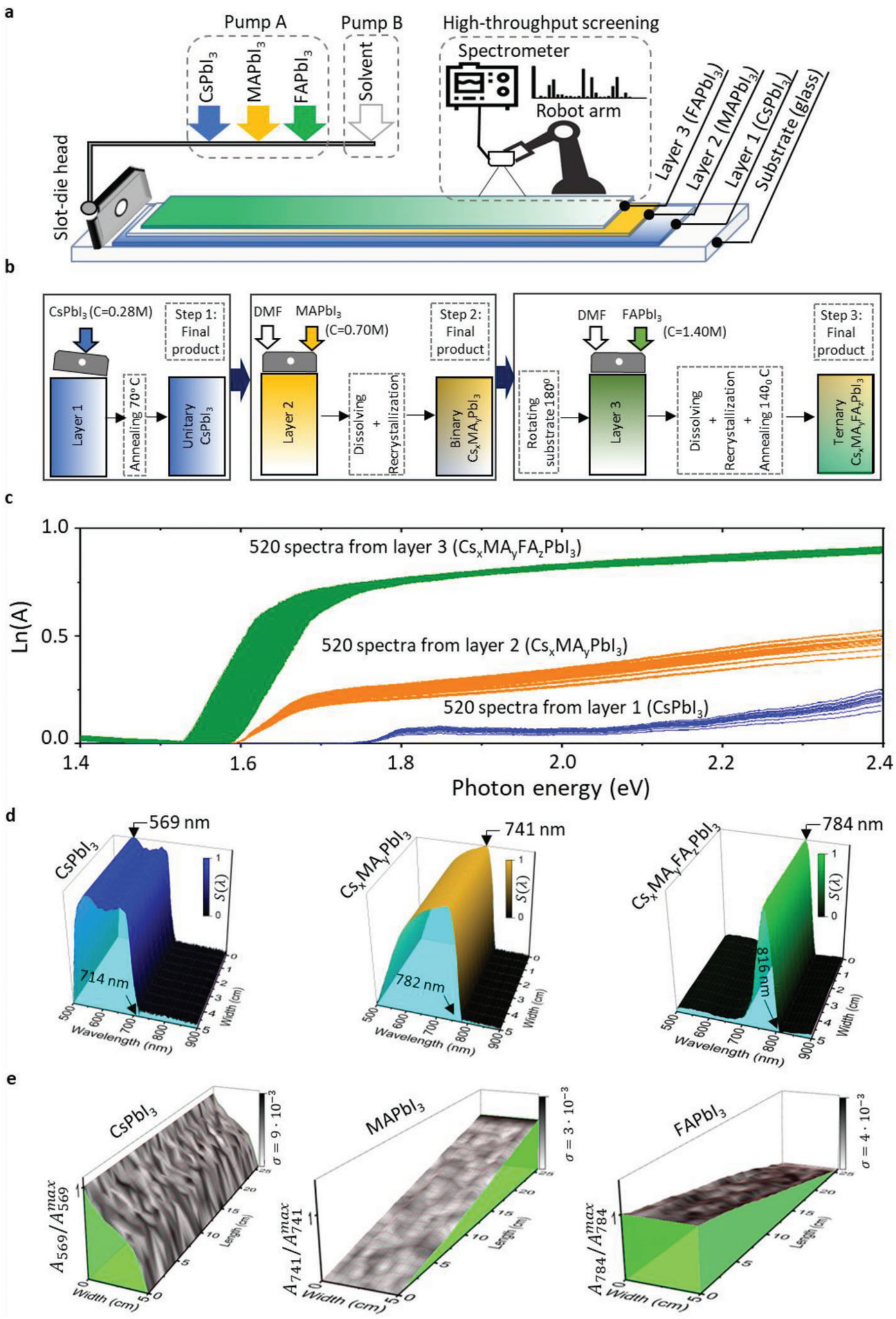

Figure 2. Fabrication of $Cs_xMA_yFA_zPbI_3$ t-CGFs. a) Schematic of sequential deposition of three layers by slot-die coating, and robotized high-throughput screening by an optical spectrometer. b) Three steps of synthesizing t-CGFs; the first layer is made by a tilted slot-die head with one pump profile to form a gradient of $CsPbI_3$ across the width of the substrate; the second and third layers are deposited by the straight slot-die head with two pump profiles to deposit gradient films of $MAPbI_3$ and $FAPbI_3$, respectively, across the length of the substrate; coating of subsequent layers dissolve previous one(s) and recrystallizing into new perovskite compositions. c) Absorption spectra after each step of fabrication. d) Variation of normalized absorbance as a function of wavelength across the film for three sequential layers. e) Normalized absorbance to global maximum showcasing gradient thickness; the gray color of the surface shows standard deviation across the film.

(Figure S2c,d, Supporting Information). Finally, $FAPbI_3$ film was deposited on top of $CsPbI_3/MAPbI_3$ sandwich film, but its thickness gradient was opposite to $MAPbI_3$.

To assess the capability of our approach in the fabrication of thickness-graded films, we measured absorption spectra for every 0.25 cm^2 segment of the substrate, which sums up to 520 locations (130/0.25 cm^2, i.e., 52 in length × 10 in width). We used a robotic arm and a reflection probe of a spectrometer to collect all spectra in 10 min (Figure S3 and Movie S1, Supporting Information). Since absorbance directly depends on the absorber's

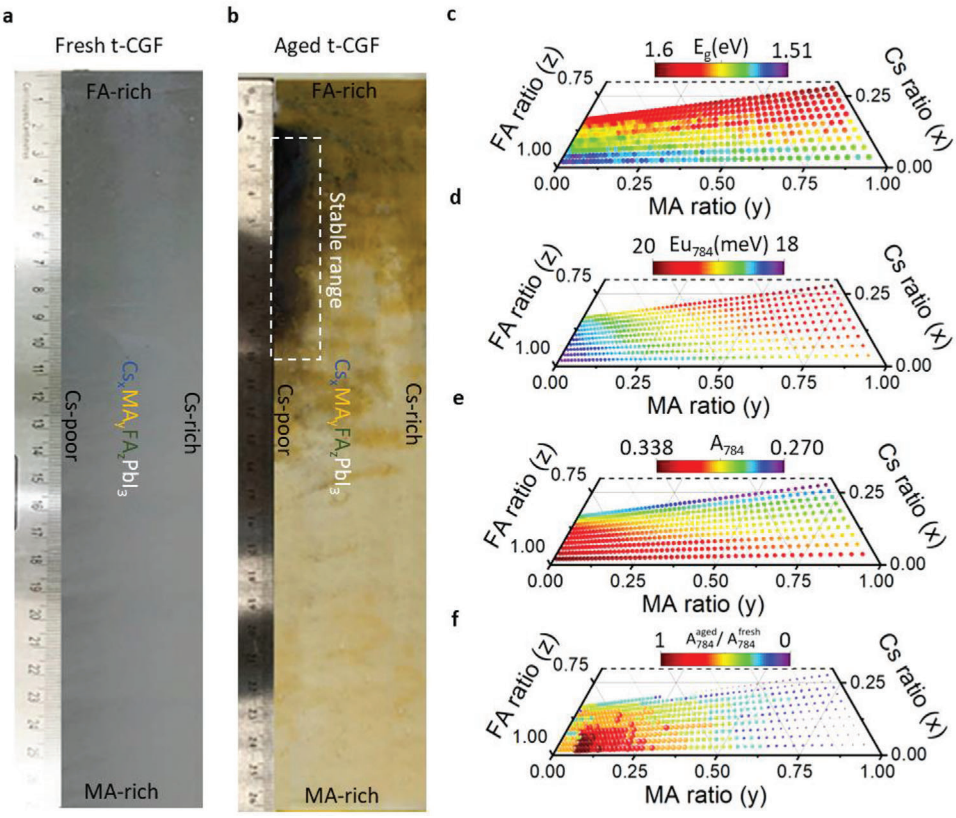

Figure 3. Stability test of $Cs_xMA_yFA_zPbI_3$ t-CGF. a) Image of fresh t-CGF of $Cs_xMA_yFA_zPbI_3$. b) Image of the same t-CGF aged for 92 days under 99% relative humidity; the dashed rectangle shows an area that experienced no/little color change. c) Bandgap of fresh t-CGF. d) Urbach energy of fresh t-CGF. e) Absorbance of fresh t-CGF. f) Ratio of absorbance values of the aged film to fresh film at 784 nm for 520 locations (compositions).

thickness (Beer–Lambert law), we used absorbance value (A) to estimate the spatial thickness of films for each deposited layer.

Figure 2c shows the absorption spectra for each layer at 520 locations. From the maximum variance of absorbance as a function of wavelength, $S(\lambda)$, along the t-CGF (Note S4, Supporting Information), we found photon wavelength that exhibits the highest sensitivity to the absorber's thickness (Figure 2d). The $S(\lambda)$ shows a clear red-shift by adding each layer indicating successful alloying of compositions in each deposition step. We used the maximum $S(\lambda)$ value to map thickness-gradient along and across the fabricated t-CGF in each step (Figure 2e). We indeed found that all three layers ($CsPbI_3$, $MAPbI_3$, and $FAPbI_3$) were deposited in a gradient fashion with a low standard deviation of $\sigma < 10^{-2}$ of relative absorbance (Figure 2e) that guarantees alloying of all designed combinatorial ratios.

The exact composition of $Cs_xMA_yFA_zPbI_3$ in a specific location of t-CGF can be determined from its spatial coordinates (just like the coordinates can be calculated from the given composition, as discussed in Note S1, Supporting Information). But we sought to validate the compositional distribution of the $Cs_xMA_yFA_zPbI_3$ t-CGF by conventional analytical methods (Note S5, Supporting Information). The ratios of organic and inorganic ions, identified by NMR and EDX, from multiple locations, show an expected trend in compositional change (Figures S4 and S5, Supporting Information). Relatively large offset of NMR values is because of the film's large area of 2.5 × 2.5 cm^2 we had to scratch to perform this analysis. Powder XRD shows single peaks corresponding to the perovskite phase indicating the successful formation of alloys (Figure S6a–c, Supporting Information), rather than multi-layered structures in which case one would expect to observe multiple perovskite diffraction peaks. We thus conclude that each subsequent slot-die-coating dissolved the previous layers and crystallized as a new alloy:

$$CsPbI_{3(l)} \xrightarrow{1} CsPbI_{3(s)} \xrightarrow{2:\ MAPbI_{3(l)}} Cs_xMA_yPbI_{3(s)} \xrightarrow{3:\ FAPbI_{3(l)}} Cs_xMA_yFA_zPbI_{3(s)} \quad (1)$$

where l and s stand for the solution and solid, respectively.

Powder XRD spectra show shrinkage of the crystal lattice parameters from FA-rich perovskite to Cs and MA-rich perovskites, again indicating the successful formation of ternary gradient film (Figure S6d, Supporting Information). In addition, the full-width at half maxima of XRD peaks indicate that the Cs-rich films are made of larger crystallites (Figure S6d, Supporting Information); this observation is further supported by surface scanning electron microscopy (SEM) images of Cs-less and Cs-containing perovskite films (Figure S7, Supporting Information). The addition of Cs leads to seeded crystallization, resulting in the formation of larger grains that offer improved stability against external factors.[52]

Figure 3a,b shows the fresh t-CGF of $Cs_xMA_yFA_zPbI_3$, and the same after it was aged at 99% relative humidity for 92 days,

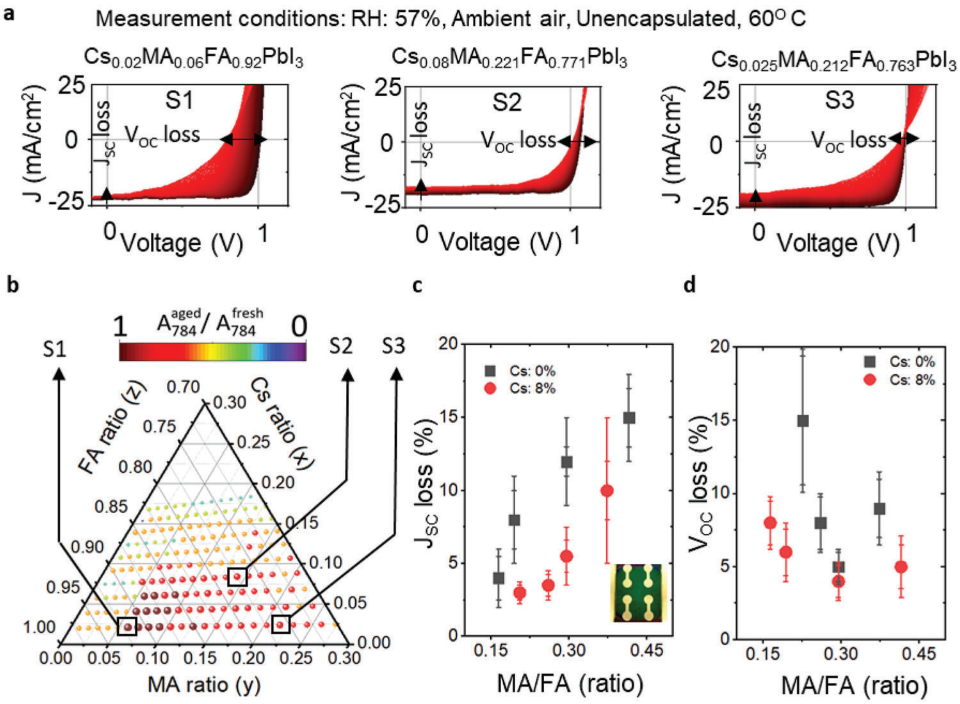

Figure 4. Operational stability of ternary perovskite solar cells. a) Evolution of current–voltage characteristics of perovskite solar cells in ambient air at ≈57% RH at 60 °C without encapsulation. b) Selected compositions from the stable region in the ternary diagram. c) Loss of short circuit current density (J_{SC}), and d) open circuit voltage (V_{OC}) as a function of perovskite composition within ¼ h of test in ambient air at ≈57% RH at 60 °C without encapsulation.

respectively. The t-CGFs provide an unprecedented dense library to study the properties and stability of alloys, unlike conventional approaches, which study only a fragment of possible compositions. We measured the bandgap and Urbach energy of fresh $Cs_xMA_yFA_zPbI_3$ alloys at 520 locations (Figure 3c,d). The bandgap, as expected, increased from ≈1.50 (eV) for FA-rich perovskite to ≈1.61 (eV) for MA- and Cs-rich perovskite. All studied $Cs_xMA_yFA_zPbI_3$ alloys, when fresh, show a relatively small Urbach energy of 19 ± 2 meV demonstrating low energy disorder and hence can be used to make performing cells.[53,54]

The humidity stress discolored a major portion of the t-CGF, while only its small area remained black (Figure 3b). To quantify the stability of ternary alloys, we measured absorbance (Figure 3e) of the fresh and aged t-CGF, and then looked at the ratio of absorbance values at 784 nm; in this analysis, more deviation of this ratio from the unity means more change or instability of the composition. The stable range shown in Figure 3b, when decoded to composition (Note S1, Supporting Information), is made of $Cs_xMA_yFA_zPbI_3$ with $x < 0.1$; $0.1 < y < 0.25$; $0.75 < z < 0.9$ (Figure 3f), with near-unity tolerance factor (Figure 1c). Figure S8, Supporting Information, shows the optoelectronic properties of the t-CGF in the real space on the substrate. We re-synthesized this stable range again and indeed confirmed that this combinational range remained black when exposed to identical humidity stress (Figure S9, Supporting Information).

Inspired by this finding of a range of stable ternary perovskites, we fabricated solar cells in a conventional architecture (Glass/ITO/SnO_2/Perovskite/Spiro-OMeTAD/Au) in ambient air. We chose three types of mono-halide perovskites from the defined stable range, which we name FA-, MA-, and Cs-rich regions (exact compositions are shown in **Figure 4** and Figure S10, Supporting Information). Our champion device showed 22.2% power conversion efficiency (Figure S11, Supporting Information) with J_{SC} of 24.7 mA cm^{-2}, V_{OC} of 1.14 V, and a FF of 79%; further optimizations (e.g., device architecture, selective carrier transport materials, and interface engineering), not the subject of this study, may lead to higher efficiencies. Although this study is focused on single-halide perovskites, we also fabricated mixed-halide perovskite solar cells ($Cs_{0.05}MA_{0.15}FA_{0.8}PbI_{2.55}Br_{0.45}$)[43]which we recently demonstrated to operate over 500 h at maximum power point at room temperature when encapsulated.

To study the stability of PSCs, we measured their current–voltage characteristics in ambient air at ≈57% RH at 60 °C without encapsulation. These conditions represent accelerated tests by a factor of ≈10^4 compared to encapsulated devices tested with no heating stress (Figure S12, Supporting Information). Then we conducted operational stability test by tracking maximum power point operation for unencapsulated solar cell devices at 60 °C (Figure S12, Supporting Information). MA-rich perovskites experience rapid loss of J_{SC} due to the loss of MA (Figure 4a), while FA-rich perovskites experience a rapid loss of V_{OC} due to polymorphism of FA-rich perovskites (Figure 4a). Cs-containing perovskites, among all, show the least loss in all photovoltaic parameters (Figure 4a) likely due to improved morphology of perovskites (Figure S7, Supporting Information). We further fabricated PSCs from six locations of the defined stable region of ternary perovskites (Figure S10, Supporting

Information). Figure 4c,d, and Figure S12, Supporting Information, show the trends as a function of composition, based on which we conclude that J_{SC} loss can be minimized with the increase of FA and Cs components, while the presence of the optimum amount of MA is needed to minimize the V_{OC} loss.

3. Conclusion

Compositional engineering is arguably a key knob in developing new materials. We reported a strategy for the synthesis of all possible ternary compositions. Applying our platform to halide perovskites, we showed a range of perovskite compositions that remained stable in moisture-supersaturated air and demonstrated their use in fabricating perovskite solar cells in ambient conditions. These compositions can be promising candidates for the commercialization of PSCs because they can be fabricated in relaxed conditions; and can be easily upscaled as they were made by a commercially-relevant slot-die coating method (Figure S13, Supporting Information). While we demonstrated the use of t-CGFs for a comprehensive exploration of ternary perovskites, this approach can be adopted for any other mixtures that can be solution-processed.

4. Experimental Section

Materials: Cesium iodide (CsI, >99.99%), *N*,*N*-dimethyl formamide (DMF, 99.5%), dimethylsulfoxide (DMSO, 99.5%), chlorobenzene (99.5%), and acetonitrile (≥99.9%), bis(trifluoromethane)sulfonimide lithium salt (Li-TFSI 99.95%) and cobalt salt (FK 209 Co(III) TFSI) were purchased from MiliporeSigma. Formamidinium iodide (FAI, >99.99%), and methylammonium iodide (MAI, >99.99%) were purchased from Greatcell Solar Materials. Lead(II) iodide (PbI_2, 99.99%) was purchased from TCI Chemicals. Tin (IV) oxide (SnO_2) 15% in H_2O colloidal dispersion solution was purchased from the Alfa Aesar. Sprio-OMeTAD was purchased from Xi'an Polymer Light Technology Co., Ltd.

Ternary CGF Fabrication: Perovskite inks were made by dissolving MAI, FAI, CsI, and PbI_2 in DMF and DMSO with the ratio of (4:1) to prepare 1.4, 0.7, and 0.28 M solutions of $FAPbI_3$, $MAPbI_3$, and $CsPbI_3$, respectively. Slot-die coating was performed on InfinityPV Research Laboratory Coater following profiles shown in Supporting Information. $CsPbI_3$ was deposited using one pump with a tilted head; first, the dead volume and the reservoir were filled, and then the film was deposited at a small speed. $MAPbI_3$ and $FAPbI_3$ were deposited in gradient thickness using two pumps. The dead volumes (from syringes to the end of the T junction) were filled with inks at a speed of 0.01 mL min^{-1}, and then the T junction was attached to the slot-die head. The time required to fill the slot-die head until the appearance of ink at the tip of the head at a speed of 0.3 mL min^{-1} was measured to be 56 s. Then the first ink supply was paused, but the second string containing DMF and DMSO with a 4:1 ratio was pumped at the same speed of 0.3 mL min^{-1}. The speed of the moving head along the 260 mm was installed to be 260 mm/56 s = 4.64 mm s^{-1} to be able to linearly dilute the stored ink in the reservoir. $MAPbI_3$ and $FAPbI_3$ were deposited in opposite directions. The first and second layers were fabricated at 70 °C; the final layer was deposited at 140 °C.

PSC Fabrication: The UV–ozone treated glass/ITO substrates were coated with SnO_2 by dropping 60 µL of mixed SnO_2:H_2O (1:6). 6 mL deionized (DI) water and 1 mL of SnO_2 15% in H_2O colloidal dispersion nanoparticles were used and then sonicated for 30 min and filtered with 0.45 µm polyvinylidene difluoride syringe filter before deposition. 60 µL of the prepared tin oxide solution was dropped and spin coated for 1 min with 3000 r.p.m. and the process was repeated twice. Then the substrate was annealed at 140 °C for 20 min and treated with UV-ozone for 15 min. Perovskite solution was prepared by dissolving 1 molar mass of combinatorial ratios of CsI, MAI, FAI, and PbI_2 in 0.666 mL of DMF:DMSO with the ratio of 1:10. Then 90 µL of mixed-cation, single-halide perovskite (1.5 M) in the ambient air was deposited by a spinner at 500 r.p.m. for 5s, 1000 r.p.m. for 5s, and 4500 r.p.m. for the 30s. During the last step, 500 µL of chlorobenzene was dropped on the film at the 30 s, followed by annealing at 140 °C for 10 min. Spiro-OMeTAD solution was prepared by dissolving 0.1 g of spiro-OMeTAD powder in 1.1 mL of chlorobenzene, 0.039 mL of tBP, 0.023 mL of Li-TFSI (dissolved in acetonitrile, 540 mg mL^{-1}), and 0.01 mL of Co-complex (dissolved in acetonitrile, 376 mg mL^{-1}) solution. Then 60 µL Spiro-OMeTAD was dynamically spin-coated for the 30 s. Finally, 70 nm gold was thermally evaporated (Angstrom Engineering). All the solutions, that is, perovskite, and spiro-OMeTAD were filtered with 0.22 µm polytetrafluoroethylene syringe filter.

Characterization: Optical characterization was carried out via a UV–vis AVENTES spectrometer (AvaSpec-ULS2048CL-EVO-RS) in the reflection mode. The absorption spectra of the gradient film were recorded in the wavelength range of 500–900 nm in ambient temperature every 150 ms. The probe of the spectrometer was attached to a robot arm. The movie shows the automating paths using Dorna 2 robotic arm (Dorna robotics) to the acquisition of ternary CGF's optical properties. The samples were aged in a humid chamber—a transparent glass box with a humidity sensor and a container of water. For XRD measurement, PANalytical Empyrean system using a Cu source (K_α, 1.5406 Å) was used. Perovskite solar cells were fabricated in ambient air. SEM images were obtained with a Hitachi S-4800 FESEM. Photovoltaic parameters were measured with Newport Oriel Sol-3A (class AAA) solar simulator at standard 1.5 A.M. Solar irradiance and data were recorded with Ossila source meter by scanning the cell from −0.1 to 1.2 V. For operational stability measurements, perovskite solar cells were placed in LED simulator and data was recorded with Ossila source meter.

Supporting Information

Supporting Information is available from the Wiley Online Library or from the author.

Acknowledgements

The authors thank the Solaires Entreprises Inc. and the Canada's Natural Sciences and Engineering Research Council (ALLRP 561355-20) for their financial support. M.I.S. is grateful to the NSERC (RGPIN-2020-04239), the Canadian Foundation for Innovation (40326), the B.C. Knowledge Development Fund (806169), and the Canada Research Chairs Program (CRC-2019-00297) for operational and infrastructure support. Y.H. thanks the Japan Society for the Promotion of Science (JSPS) Overseas Research Fellow program for their financial support.

Conflict of Interest

The authors declare no conflict of interest.

Data Availability Statement

The data that support the findings of this study are available in the supplementary material of this article.

Keywords

functional materials, high-throughput, perovskites

Received: February 6, 2023
Revised: May 22, 2023

[1] A. Harillo-Baños, Q. Fan, S. Riera-Galindo, E. Wang, O. Inganäs, M. Campoy-Quiles, *ChemSusChem* **2022**, *15*, 202101888.

[2] S. Moradi, S. Kundu, M. I. Saidaminov, *ACS Mater. Au* **2022**, *2*, 516.

[3] H. Näsström, O. Shargaieva, P. Becker, F. Mathies, I. Zizak, V. R. F. Schröder, E. J. W. List-Kratochvil, T. Unold, E. Unger, *J. Mater. Chem. A* **2022**, *10*, 4906.

[4] S. Moradi, S. Kundu, M. Rezazadeh, V. Yeddu, O. Voznyy, M. I. Saidaminov, *Commun. Mater.* **2022**, *3*, 13.

[5] Y. Zhao, T. Heumueller, J. Zhang, J. Luo, O. Kasian, S. Langner, C. Kupfer, B. Liu, Y. Zhong, J. Elia, A. Osvet, J. Wu, C. Liu, Z. Wan, C. Jia, N. Li, J. Hauch, C. J. Brabec, *Nat. Energy* **2021**, *7*, 144.

[6] Y. An, C. A. R. Perini, J. Hidalgo, A.-F. Castro-Méndez, J. N. Vagott, R. Li, W. A. Saidi, S. Wang, X. Li, J.-P. Correa-Baena, *Energy Environ. Sci.* **2021**, *14*, 6638.

[7] Y. Zhao, J. Zhang, Z. Xu, S. Sun, S. Langner, N. T. P. Hartono, T. Heumueller, Y. Hou, J. Elia, N. Li, G. J. Matt, X. Du, W. Meng, A. Osvet, K. Zhang, T. Stubhan, Y. Feng, J. Hauch, E. H. Sargent, T. Buonassisi, C. J. Brabec, *Nat. Commun.* **2021**, *12*, 2191.

[8] D. Ulkoski, M. J. Munson, M. E. Jacobson, C. R. Palmer, C. S. Carson, A. Sabirsh, J. T. Wilson, V. R. Krishnamurthy, *ACS Appl. Bio Mater.* **2021**, *4*, 1640.

[9] X. Rodríguez-Martínez, E. Pascual-San-José, M. Campoy-Quiles, *Energy Environ. Sci.* **2021**, *14*, 3301.

[10] Y. Zhao, J. Zhang, Z. Xu, S. Sun, S. Langner, N. T. P. Hartono, T. Heumueller, Y. Hou, J. Elia, N. Li, G. J. Matt, X. Du, W. Meng, A. Osvet, K. Zhang, T. Stubhan, Y. Feng, J. Hauch, E. H. Sargent, T. Buonassisi, C. J. Brabec, *Nat. Commun.* **2021**, *12*, 2191.

[11] S. Jiang, J. Song, Y. Zhang, M. Nie, J. Kim, A. L. Marcano, K. Kadlec, W. A. Mills, X. Yan, H. Liu, R. Tong, H. Wang, I. F. Kimbrough, H. Sontheimer, W. Zhou, X. Jia, *ACS Appl. Mater. Interfaces* **2021**, *13*, 9156.

[12] Z. Wang, B. Xie, Q. Fang, F. Liu, J. Li, L. Tan, Z. Huang, L. Zhao, L. Jiang, *MRS Commun.* **2021**, *11*, 411.

[13] A. Nandy, C. Duan, M. G. Taylor, F. Liu, A. H. Steeves, H. J. Kulik, *Chem. Rev.* **2021**, *121*, 9927.

[14] D. Song, X. Chen, Z. Lin, Z. Tang, W. Ma, Q. Zhang, Y. Li, X. Zhang, *ACS Nano* **2021**, *15*, 16469.

[15] T. Bo, Y. Wang, Y. Liang, X. Liu, J. Ren, H. Weng, M. Liu, S. Meng, *J. Phys. Chem. Lett.* **2021**, *12*, 6667.

[16] J. L. Hitt, Y. C. Li, S. Tao, Z. Yan, Y. Gao, S. J. L. Billinge, T. E. Mallouk, *Nat. Commun.* **2021**, *12*, 1114.

[17] D. Ulkoski, M. J. Munson, M. E. Jacobson, C. R. Palmer, C. S. Carson, A. Sabirsh, J. T. Wilson, V. R. Krishnamurthy, *ACS Appl. Bio Mater.* **2021**, *4*, 1640.

[18] G. L. W. Hart, T. Mueller, C. Toher, S. Curtarolo, *Nat. Rev. Mater.* **2021**, *6*, 730.

[19] Y. Sheng, T. Deng, P. Qiu, X. Shi, J. Xi, Y. Han, J. Yang, *Chem. Mater.* **2021**, *33*, 6918.

[20] X. Du, L. Lüer, T. Heumueller, J. Wagner, C. Berger, T. Osterrieder, J. Wortmann, S. Langner, U. Vongsaysy, M. Bertrand, N. Li, T. Stubhan, J. Hauch, C. J. Brabec, *Joule* **2021**, *5*, 495.

[21] A. J. Gormley, M. A. Webb, *Nat. Rev. Mater.* **2021**, *6*, 642.

[22] R. Upadhya, S. Kosuri, M. Tamasi, T. A. Meyer, S. Atta, M. A. Webb, A. J. Gormley, *Adv. Drug Delivery Rev.* **2021**, *171*, 1.

[23] Q. Wang, L. Velasco, B. Breitung, V. Presser, *Adv. Energy Mater.* **2021**, *11*, 2102355.

[24] S. Liang, *Comb. Chem. High Throughput Screening* **2021**, *24*, 891.

[25] S. Langner, F. Häse, J. D. Perea, T. Stubhan, J. Hauch, L. M. Roch, T. Heumueller, A. Aspuru-Guzik, C. J. Brabec, *Adv. Mater.* **2020**, *32*, 1907801.

[26] A. Harillo-Baños, X. Rodríguez-Martínez, M. Campoy-Quiles, *Adv. Energy Mater.* **2020**, *10*, 1902417.

[27] J. G. Manion, A. H. Proppe, G. E. J. J. Hicks, E. H. Sargent, D. S. Seferos, *ACS Appl. Mater. Interfaces* **2020**, *12*, 26026.

[28] N. Kumari Jangid, S. Jadoun, N. Kaur, *Eur. Polym. J.* **2020**, *125*, 109485.

[29] T. H. Piotrowiak, X. Wang, L. Banko, S. Kumari, S. Sarker, A. Mehta, A. Ludwig, *ACS Comb. Sci.* **2020**, *22*, 804.

[30] S. Sun, N. T. P. Hartono, Z. D. Ren, F. Oviedo, A. M. Buscemi, M. Layurova, D. X. Chen, T. Ogunfunmi, J. Thapa, S. Ramasamy, C. Settens, B. L. DeCost, A. G. Kusne, Z. Liu, S. I. P. Tian, I. M. Peters, J.-P. Correa-Baena, T. Buonassisi, *Joule* **2019**, *3*, 1437.

[31] A. Ludwig, *npj Comput. Mater.* **2019**, *5*, 70.

[32] S. Ekins, A. C. Puhl, K. M. Zorn, T. R. Lane, D. P. Russo, J. J. Klein, A. J. Hickey, A. M. Clark, *Nat. Mater.* **2019**, *18*, 435.

[33] B. P. MacLeod, F. G. L. Parlane, T. D. Morrissey, F. Häse, L. M. Roch, K. E. Dettelbach, R. Moreira, L. P. E. Yunker, M. B. Rooney, J. R. Deeth, V. Lai, G. J. Ng, H. Situ, R. H. Zhang, M. S. Elliott, T. H. Haley, D. J. Dvorak, A. Aspuru-Guzik, J. E. Hein, C. P. Berlinguette, *Sci. Adv.* **2020**, *6*, eaaz8867.

[34] J. Burschka, N. Pellet, S.-J. Moon, R. Humphry-Baker, P. Gao, M. K. Nazeeruddin, M. Grätzel, *Nature* **2013**, *499*, 316.

[35] M. M. Lee, J. Teuscher, T. Miyasaka, T. N. Murakami, H. J. Snaith, *Science* **2012**, *338*, 643.

[36] H.-S. Kim, C.-R. Lee, J.-H. Im, K.-B. Lee, T. Moehl, A. Marchioro, S.-J. Moon, R. Humphry-Baker, J.-H. Yum, J. E. Moser, M. Grätzel, N.-G. Park, *Sci. Rep.* **2012**, *2*, 591.

[37] J.-H. Im, C.-R. Lee, J.-W. Lee, S.-W. Park, N.-G. Park, *Nanoscale* **2011**, *3*, 4088.

[38] A. Kojima, K. Teshima, Y. Shirai, T. Miyasaka, *J. Am. Chem. Soc.* **2009**, *131*, 6050.

[39] J. J. Yoo, G. Seo, M. R. Chua, T. G. Park, Y. Lu, F. Rotermund, Y. K. Kim, C. S. Moon, N. J. Jeon, J. P. Correa-Baena, V. Bulović, S. S. Shin, M. G. Bawendi, J. Seo, *Nature* **2021**, *590*, 587.

[40] A. Sandström, H. F. Dam, F. C. Krebs, L. Edman, *Nat. Commun.* **2012**, *3*, 1002.

[41] N. J. Jeon, J. H. Noh, W. S. Yang, Y. C. Kim, S. Ryu, J. Seo, S. Il Seok, *Nature* **2015**, *517*, 476.

[42] M. I. Saidaminov, A. L. Abdelhady, B. Murali, E. Alarousu, V. M. Burlakov, W. Peng, I. Dursun, L. Wang, Y. He, G. Maculan, A. Goriely, T. Wu, O. F. Mohammed, O. M. Bakr, *Nat. Commun.* **2015**, *6*, 7586.

[43] M. Awais, D. T. Gangadharan, F. Tan, M. I. Saidaminov, *Chem. Mater.* **2022**, *34*, 8112.

[44] S. S. Mali, J. V. Patil, J. A. Steele, S. R. Rondiya, N. Y. Dzade, C. K. Hong, *ACS Energy Lett.* **2021**, *6*, 778.

[45] K. Xiao, R. Lin, Q. Han, Y. Hou, Z. Qin, H. T. Nguyen, J. Wen, M. Wei, V. Yeddu, M. I. Saidaminov, Y. Gao, X. Luo, Y. Wang, H. Gao, C. Zhang, J. Xu, J. Zhu, E. H. Sargent, H. Tan, *Nat. Energy* **2020**, *5*, 870.

[46] K. Higgins, S. M. Valleti, M. Ziatdinov, S. V. Kalinin, M. Ahmadi, *ACS Energy Lett.* **2020**, *5*, 3426.

[47] W. Yang, W. Wang, Y. Wang, R. Sun, J. Guo, H. Li, M. Shi, J. Guo, Y. Wu, T. Wang, G. Lu, C. J. Brabec, Y. Li, J. Min, *Joule* **2021**, *5*, 1209.

[48] J. Dagar, M. Fenske, A. Al-Ashouri, C. Schultz, B. Li, H. Köbler, R. Munir, G. Parmasivam, J. Li, I. Levine, A. Merdasa, L. Kegelmann, H. Näsström, J. A. Marquez, T. Unold, D. M. Többens, R. Schlatmann, B. Stegemann, A. Abate, S. Albrecht, E. Unger, *ACS Appl. Mater. Interfaces* **2021**, *13*, 13022.

[49] K. Suchan, J. Just, P. Beblo, C. Rehermann, A. Merdasa, R. Mainz, I. G. Scheblykin, E. Unger, *Adv. Funct. Mater.* **2022**, *33*, 2206047.

[50] M. H. Futscher, J. M. Lee, L. McGovern, L. A. Muscarella, T. Wang, M. I. Haider, A. Fakharuddin, L. Schmidt-Mende, B. Ehrler, *Mater. Horiz.* **2019**, *6*, 1497.

[51] M. T. Sebastian, in *Dielectric Materials for Wireless Communication*, Elsevier, New York **2008**, pp. 161–203.

[52] Y. Zhao, H. Tan, H. Yuan, Z. Yang, J. Z. Fan, J. Kim, O. Voznyy, X. Gong, L. N. Quan, C. S. Tan, J. Hofkens, D. Yu, Q. Zhao, E. H. Sargent, *Nat. Commun.* **2018**, *9*, 1607.

[53] S. De Wolf, J. Holovsky, S.-J. Moon, P. Löper, B. Niesen, M. Ledinsky, F.-J. Haug, J.-H. Yum, C. Ballif, *J. Phys. Chem. Lett.* **2014**, *5*, 1035.

[54] E. Ugur, M. Ledinský, T. G. Allen, J. Holovský, A. Vlk, S. De Wolf, *J. Phys. Chem. Lett.* **2022**, *13*, 7702.